DOI: 10.1002/ejic.200600306

Syntheses, Structural, and Physical Studies of Basic Cr^{III} and Fe^{III} Benzilates and Benzoates: Evidence of Antisymmetric Exchange and Distributions of Isotropic and Antisymmetric Exchange Parameters

Vassilios Psycharis,*[a] Catherine P. Raptopoulou,[a] Athanassios K. Boudalis,[a] Yiannis Sanakis,[a] Michael Fardis,[a] George Diamantopoulos,[a] and George Papavassiliou[a]

Dedicated to Professor Jean-Pierre Tuchagues on the occasion of his 65th birthday

Keywords: Trinuclear oxo-centered chromium(III) and iron(III) complexes / Magnetic properties / Crystal structures / EPR spectroscopy / Mössbauer spectroscopy

The synthesis, crystal structures, spectroscopic and magnetic properties studies of four trinuclear oxo-centered carboxylate complexes are reported and discussed: $[Cr_3(\mu_3\text{-}O)\{O_2C(OH)Ph_2\}_6(H_2O)_3](NO_3)\cdot 2H_2O\cdot 3Me_2CO$ ($\mathbf{1}\cdot 2H_2O\cdot 3Me_2CO$), $[Cr_3(\mu_3\text{-}O)(O_2CPh)_6(H_2O)_3](NO_3)\cdot 1.9MeCN\cdot 0.5H_2O$ ($\mathbf{2}\cdot 1.9MeCN\cdot 0.5H_2O$), $[Fe_3(\mu_3\text{-}O)\{O_2C(OH)Ph_2\}_6(H_2O)_3](NO_3)\cdot 5.69H_2O$ ($\mathbf{3}\cdot 5.69H_2O$), and $[Fe_3(\mu_3\text{-}O)(O_2CPh)_6(H_2O)_3](NO_3)\cdot 3MeCN$ ($\mathbf{4}\cdot 3MeCN$). From a crystallographic point of view, the three metal ions form an isosceles triangle in **1** and **3** (benzilato complexes) and an almost equilateral one in **2** and **4** (benzoato complexes). Magnetic susceptibility measurements reveal metal-dependent isotropic exchange, for the Cr^{III} clusters (**1**, **2**), with the "magnetic symmetry" resembling that of an almost equilateral triangle. For the Fe^{III} clusters the "magnetic symmetry" resembles that of an isosceles triangle. Solid-state ^1H NMR studies for **1**, through the measurements of the temperature variation of the relaxation rate $1/T_1$, reveal that the first excited spin state with $S_T = 3/2$ is well above (ca. 30 cm^{-1}) the ground state with $S_T = 1/2$, consistent with the magnetic susceptibility data. Mössbauer spectroscopic studies give a larger quadrupole splitting, ΔE_Q, value for **3** than for **4**, because of a larger charge asymmetry in **3** attributed to the different nature of the carboxylato ligands. EPR experiments at X-band reveal the presence of antisymmetric exchange within the Cr^{III} clusters and distributions of both isotropic and antisymmetric exchange interactions. In the case of **2** the magnitude and distribution of these interactions are greater. EPR spectroscopy for **3** suggests weak interactions between neighboring units, which could be described assuming a dimer of trimers. For complex **4** the EPR spectra indicate a more complicated picture.

Introduction

One of the reasons for the extensive study of trinuclear oxo-centered metal carboxylate assemblies (also known as "basic carboxylates") of the general formula $[M^{III}{}_3O(O_2CR)_6L_3]^+$ (M = 3d metal ion, L = monodentate terminal ligand) is that they serve as simple systems for the study of magnetic and electronic interactions between transition-metal ions.[1–5] Additional interest originates from the fact that they are used as precursors for the synthesis of higher nuclearity clusters exhibiting interesting magnetic properties.[6,7] Such clusters are also studied because they serve as models for the building blocks of polynuclear cores in proteins[8] and in the case of Cr^{III} complexes, for their biological activity.[9]

Magnetic susceptibility studies have been performed for many "basic carboxylates",[3] and at least in the 200–300 K temperature range[1] they are well understood within the framework of the Heisenberg–Dirac–van Vleck (HDvV) isotropic spin Hamiltonian with antiferromagnetic interactions. Kambe[1] has interpreted the magnetic susceptibility data assuming that the exchange interactions within the triangle were all equal (equilateral model) or that one was different from the other two (isosceles model). The crystal structure for many trinuclear complexes reveals an equilateral configuration. Magnetostructural correlations suggest that the equilateral geometry would be appropriate for the description of the magnetic susceptibility data. However, even in highly symmetric cases the magnetic susceptibility measurements require the adoption of the isosceles configuration, in particular for the interpretation of the low-temperature properties of these systems.

The equilateral magnetic model leads to an energy-level diagram with a ground state consisting of two Kramers

---

[a] Institute of Materials Science, N.C.S.R. "Demokritos", 15310 Aghia Paraskevi, Athens, Greece

Supporting information for this article is available on the WWW under http://www.eurjic.org or from the author.

doublets. Lowering of the magnetic symmetry to the isosceles configuration indicated by the analysis of the magnetic susceptibility measurements has the consequence that these two doublets differ in energy. Experimental techniques such as heat capacity measurements[10] or inelastic neutron scattering[11,12] have confirmed the lift of the degeneracy of the ground state in consistency with a lower than equilateral geometry. In the case of Fe^{III} complexes, Mössbauer spectroscopy at liquid helium temperatures and in the presence of external magnetic fields has led to the same conclusions; the spectra obtained could not be analyzed within the framework of equilateral configuration. Instead, the spectra were reproduced by assuming lower symmetry and in some cases a scalene configuration was considered more appropriate.[13]

In order to interpret the lifting of the ground-state fourfold degeneracy, a variety of models with different physical origins has been suggested. An early model introduced the concept of the magnetic Jahn–Teller effect, within which the ground state of the system, occupied at low temperatures, adopts an isosceles rather than an equilateral configuration.[14] An isotropic model involving dynamic distortions has been suggested[15] and the results are comparable to those obtained from Kambe's static isosceles model. Other models are based on Hamiltonians that include non-Heisenberg terms and retaining, or not, the D_3 symmetry of the cluster. These are biquadratic,[16] anisotropic,[16] and antisymmetric exchange.[2,4,5,17–23] Their appearance is generally associated with spin-orbit coupling and has been adequately described.[20]

Compelling evidence for the role of antisymmetric exchange in trinuclear clusters has been provided by EPR spectroscopy. Within the context of isotropic Heisenberg interactions the $S = 1/2$ ground state would give rise to EPR spectra characterized by the anisotropy of the intrinsic g-tensors of the single ions. In the case of Cr^{III} and Fe^{III} complexes this intrinsic anisotropy is small and spectra confined in a narrow region at $g \approx 1.9–2.0$ are expected. However, the observed spectra from many clusters exhibit significant g-anisotropy, and resonances with g values significantly smaller ($g_{\text{eff}} < 1.7$) than those expected are observed.[18,19] Involvement of the antisymmetric exchange term has led to a successful interpretation of this behavior. Similarly, unexpectedly large anisotropies attributed to antisymmetric exchange have been recently observed in trinuclear Cu^{II} complexes[24] and are also frequently encountered in $[3Fe4S]^{1+}$ clusters in proteins.[25]

In some cases analysis of the X-band EPR spectra suggests that, apart from the role of antisymmetric exchange, the role of distributions of the Heisenberg and non-Heisenberg exchange coupling parameters is also of special importance.[25–27] Such distributions have also been implied from Mössbauer studies in the case of Fe^{III} complexes.[13,25,28] Inelastic neutron scattering studies with the spectral characteristics at low temperature have been explained assuming that more than one triangular complex with different degrees of symmetry-lowering are present in the structure.[12]

In the present work, we study the effect of metal and ligand variation (Cr^{III} vs. Fe^{III} and benzilates vs. benzoates) on the structural and electronic (magnetic, spectroscopic) characteristics of "basic metal carboxylates". We present the syntheses and studies of the basic benzilates and benzoates $[Cr_3(\mu_3\text{-}O)\{O_2C(OH)Ph_2\}_6(H_2O)_3](NO_3)\cdot 2H_2O\cdot 3Me_2CO$ ($\mathbf{1}\cdot 2H_2O\cdot 3Me_2CO$), $[Cr_3(\mu_3\text{-}O)(O_2CPh)_6(H_2O)_3](NO_3)\cdot 1.9MeCN\cdot 0.5H_2O$ ($\mathbf{2}\cdot 1.9MeCN\cdot 0.5H_2O$), $[Fe_3(\mu_3\text{-}O)\{O_2C(OH)Ph_2\}_6(H_2O)_3](NO_3)\cdot 5.69H_2O$ ($\mathbf{3}\cdot 5.69H_2O$), and $[Fe_3(\mu_3\text{-}O)(O_2CPh)_6(H_2O)_3](NO_3)\cdot 3MeCN$ ($\mathbf{4}\cdot 3MeCN$). In particular we present structural, magnetic and X-band EPR data for **1**–**4**, Mössbauer spectroscopic data for **3** and **4** and solid-state NMR spectroscopic data for **1**. This is a continuation of our work on Cr^{III}[26] and Fe^{III}[27,29–31] complexes exhibiting phenomena like spin frustration, antisymmetric exchange, and J-strain, studied with spectroscopic techniques such as EPR.

Results and Discussion

Syntheses

Most Cr^{III} "basic carboxylate" complexes have in general been prepared by complicated synthetic routes yielding intractable solids or liquids.[3] Fe^{III} "basic carboxylates" have been prepared by reaction of a Fe^{III} salt with the appropriate sodium carboxylate in aqueous solutions, yielding amorphous solids. In any case, pure crystalline products could not be isolated without recrystallization from organic solvents. Thus, we have reacted Cr^{III} and Fe^{III} salts with the appropriate carboxylic acid or sodium salt directly in organic solvents and we have isolated the corresponding "basic carboxylates" in crystalline form following a straightforward and simple synthetic procedure.

The balanced chemical equations for the synthesis of the "basic benzilates" (Cr^{III}: **1**, Fe^{III}: **3**) and the "basic benzoates" (Cr^{III}: **2**, Fe^{III}: **4**) may be written in the forms of Equations (1) and (2) respectively. In every case it is assumed that H_2O from the starting materials and/or the solvent is the source of the O^{2-} ion.

$$3\,M(NO_3)_3\cdot 9\,H_2O + 6\,Ph_2C(OH)COOH \xrightarrow{Me_2CO\,(\mathbf{1}),\,CH_2Cl_2\,(\mathbf{3})} [M_3O\{O_2C(OH)Ph_2\}_6(H_2O)_3](NO_3) + 8\,HNO_3 + 23\,H_2O \quad M = Cr\,(\mathbf{1}),\,Fe\,(\mathbf{3}) \tag{1}$$

$$3\,M(NO_3)_3\cdot 9\,H_2O + 6\,PhCO_2Na \xrightarrow{MeCN\,(\mathbf{2},\mathbf{4})} [M_3O(PhCO_2)_6(H_2O)_3](NO_3) + 6\,NaNO_3 + 2\,HNO_3 + 23\,H_2O \quad M = Cr\,(\mathbf{2}),\,Fe\,(\mathbf{4}) \tag{2}$$

A point of synthetic interest is that for the carboxylates at hand, the use of the carboxylic acid (**1**/**3**) or the sodium carboxylate (**2**/**4**) have both led to the desired complexes.

Table 1. Selected bond lengths [Å] and angles [°] for **1**–**4**.[a]

	1	**2**	**3**	**4**
M–O_{oxo}	1.904(3)–1.907(3)	1.887(4)–1.899(4)	1.893(6)–1.935(6)	1.898(6)–1.908(7)
M–$O_{carboxylato}$	1.959(3)–1.990(3)	1.947(4)–1.980(5)	1.991(6)–2.036(7)	1.977(8)–2.029(9)
M–O_{H_2O}	2.008(5)–2.024(5)	2.025(5)–2.067(6)	2.035(7)–2.133(6)	2.082(8)–2.112(7)
M···M	3.278(3)–3.314(3)	3.276(4)–3.290(4)	3.280(6)–3.333(6)	3.290(8)–3.298(8)
M–O_{oxo}–M	118.8(2)–120.9(2)	119.3(2)–120.8(2)	119.3(3)–121.1(3)	119.6(4)–120.5(4)

[a] M = Cr (**1**, **2**), Fe (**3**, **4**).

Description of the Structures

General Remarks

Compounds **1**–**4**, as members of the large family of "basic carboxylates" containing a central planar $[M_3(\mu_3\text{-}O)]^{7+}$ core and the carboxylato ligands, lie above and below this plane. The monodentate ligands are directed *trans* to the Fe–O_{oxo} bonds. Their structural parameters are typical of "basic carboxylates" and will not be analyzed in detail. In the case of the benzilato complexes **1** and **3**, the triangles formed by the three metal ions are best described as isosceles, while in the benzoato complexes **2** and **4** the triangles formed are equilateral (within a few standard deviations). Selected bond lengths and angles for **1**–**4** are listed in Table 1, and the molecular structure of **1** is selectively shown in Figure 1. The most interesting feature in the structures of **1**–**4** is the presence of intermolecular interactions and the formation of 2D networks, which will be discussed in detail.

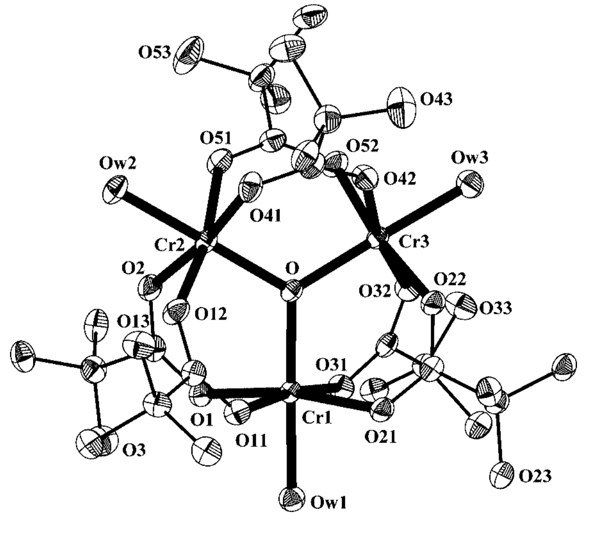

Figure 1. Partially labeled ORTEP plot of the cation of **1** with ellipsoids drawn at the 40% probability level. Only the *ipso* carbon atoms of the benzilato ligands are shown and hydrogen atoms have been omitted for clarity.

Lattice Structure of 1·2H$_2$O·3Me$_2$CO

As shown in Figure 2, the cations of **1** are hydrogen-bonded through their aquo ligands [Ow(1), Ow(2) and Ow(3)] to the nitrate counterions and the solvate molecules [Ow(4), Ow(5) and acetone solvates]. In particular, the water solvate Ow(5) is the intermediate through which the trimers are connected to each other through the hydrogen bonds to Ow(2) and O(53) of one trimer [Ow(5)···O(w2) 2.642 Å, Ow(5)···O(53) 2.977 Å] and O(23) of a neighboring one [Ow(5)···O(23′) 2.809 Å (1 + *x*, *y*, *z*)] forming chains parallel to the *a* axis of the unit cell. The nitrate counterions link trimers belonging to neighboring chains resulting in the formation of layers extended along the *ab* plane [O(33)···O(62′′) 3.001 Å (0.5 – *x*, –0.5 + *y*, 0.5 – *z*), Ow(3)···O(62′′) 2.741 Å (0.5 – *x*, –0.5 + *y*, 0.5 – *z*), O(3)···O(61′′′) 2.885 Å (*x*, –1 + *y*, *z*), Ow(1)···O(61′′′) 2.659 Å (*x*, –1 + *y*, *z*)]. The three acetone and the second water solvate molecules are hydrogen-bonded to each other and to coordinated water molecules as well as to the hydroxy group of the benzilato ligands, thus further stabilizing the above-mentioned 2D network.

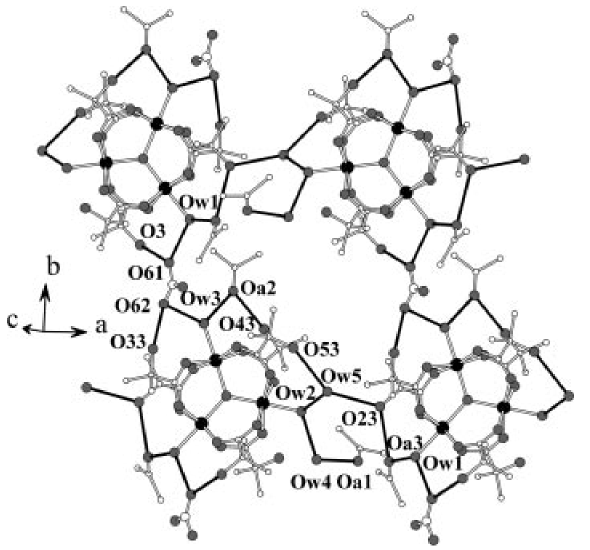

Figure 2. Plot of the 2D polymeric structure of **1** parallel to the *ab* plane. Hydrogen bonds are shown as thick black lines (only the *ipso* carbon atoms of the benzilato ligands are shown). Cr: black circles, O: dark gray, N: large open circles, C: small open circles.

Lattice Structure of 2·1.9MeCN·0.5H$_2$O

The lattice structure of **2** due to hydrogen-bonding interactions is shown in Figure 3. The key feature is the presence of the nitrate counterion, which is hydrogen-bonded to the coordinated water molecules of three different trimers [O(61)···Ow(1′) 2.908 Å (–1 + *x*, *y*, *z*), O(62)···Ow(2′′) 2.875 Å (*x*, –1 + *y*, *z*), O(63)···Ow(3) 2.901 Å]. Thus, a 2D network is formed that is parallel to the *ab* plane. The solvate molecules are hydrogen-bonded to each other and to coordinated water molecules but they do not contribute to the formation of a further polymeric network (these interactions are not shown in Figure 3).

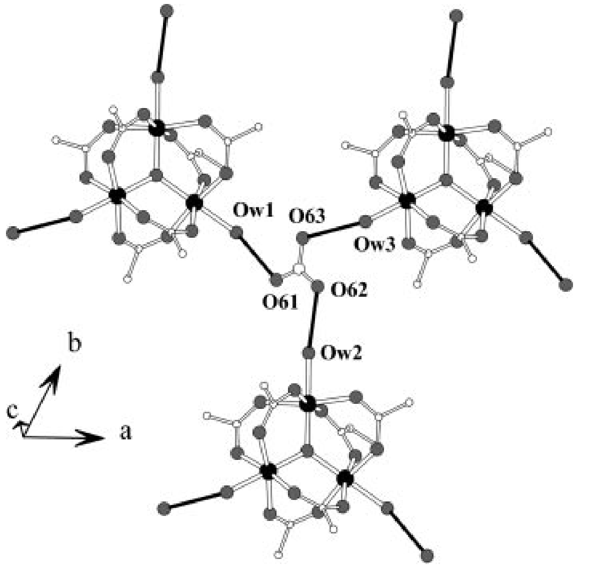

Figure 3. Plot of the 2D polymeric structure of **2** parallel to the *ab* plane. Hydrogen bonds are shown as thick black lines. (only the *ipso* carbon atoms of the benzoato ligands are shown). Cr: black circles, O: dark gray, N: large open circles, C: small open circles.

Lattice Structure of 3·5.69H$_2$O

In the structure of **3**, the X-ray analysis could not reveal the hydrogen atoms of the aquo and benzilato ligands, thus only the intermolecular interactions will be considered for the formation of the lattice structure (Figure 4). Strong intermolecular interactions between O(53) of one trimer and O(13) and Ow(2) of a neighboring trimer [O(53)··· O(13′) 2.917 Å (1.5 – *x*, 0.5 – *y*, 1 – *z*), O(53)···Ow(2′) 2.917 Å (1.5 – *x*, 0.5 – *y*, 1 – *z*)] are responsible for the formation of dimers of trimers. The presence of the nitrate counterions and the existence of strong intermolecular interactions [O(61)···Ow(1′′) 2.668 Å (–0.5 + *x*, 0.5 + *y*, *z*) and O(63)···Ow(3′′′) 2.612 Å (1 – *x*, *y*, 0.5 – *z*)] connects the dimers together and the final result is the formation of a 2D polymeric network parallel to the *bc* plane.

Lattice Structure of 4·3MeCN

As in the case of **3**, the X-ray crystal structure analysis of **4** did not reveal the hydrogen atoms of the aquo ligands. Nevertheless, intermolecular interactions less than 3 Å with the nitrate counterions are considered as possible hydrogen-bonding interactions. In particular, the nitrate anions interact with three neighboring trimers [O(61)···Ow(3′) 2.890 Å (1 – *x*, –*y*, 1 – *z*), O(62)···Ow(1′′) 2.680 Å (0.5 – *x*, –0.5 + *y*, 1 – *z*), O(63)···Ow(2′′′) 2.798 Å (0.5 – *x*, 0.5 + *y*, 1 – *z*)], linking the trimers to form a 2D polymeric network parallel to the *ab* plane (Figure 5). The solvent molecules of crystallization also interact intermolecularly with the coordinated water molecules, but they do not contribute to a further development of the lattice structure (these interactions are not shown in Figure 5).

Mössbauer Spectroscopy

Mössbauer spectra from solid powder samples of **3** and **4** were recorded at zero magnetic field in the 78–300 K temperature range. The spectra at 78 K are shown in Figure 6. Each compound gives rise to one doublet with the following values for the quadrupole interaction (ΔE_{Q}) and the isomer shift (δ): complex **3**, ΔE_{Q} = 0.65 mm s^{-1}, δ = 0.50 mm s^{-1}; complex **4**, ΔE_{Q} = 0.52 mm s^{-1}, δ = 0.52 mm s^{-1}. The values for the isomer shift are consistent with Fe$^{\mathrm{III}}$ (S = 5/2) in

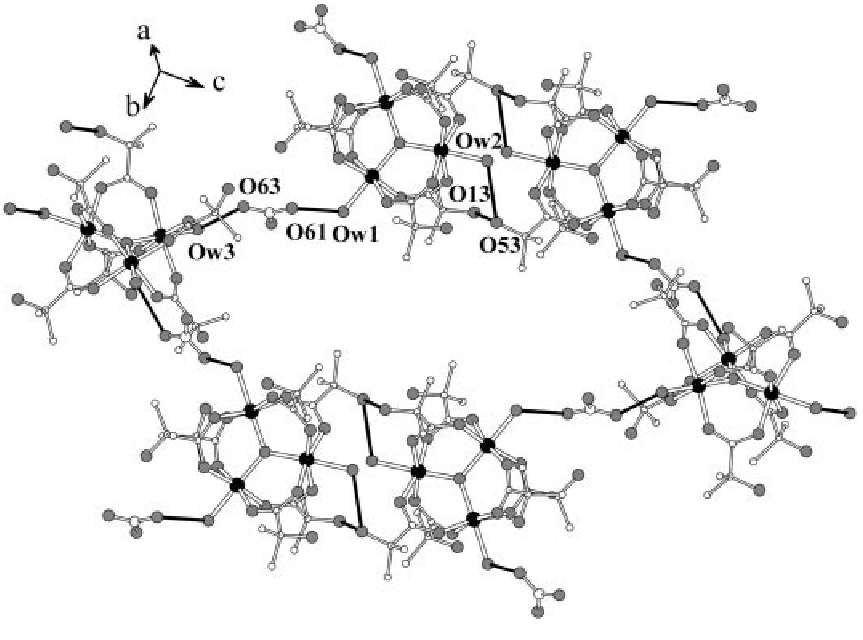

Figure 4. Plot of the 2D polymeric structure of **3** parallel to the *bc* plane. Hydrogen bonds are shown as thick black lines (only the *ipso* carbon atoms of the benzilato ligands are shown). Fe: black circles, O: dark gray, N: large open circles, C: small open circles.

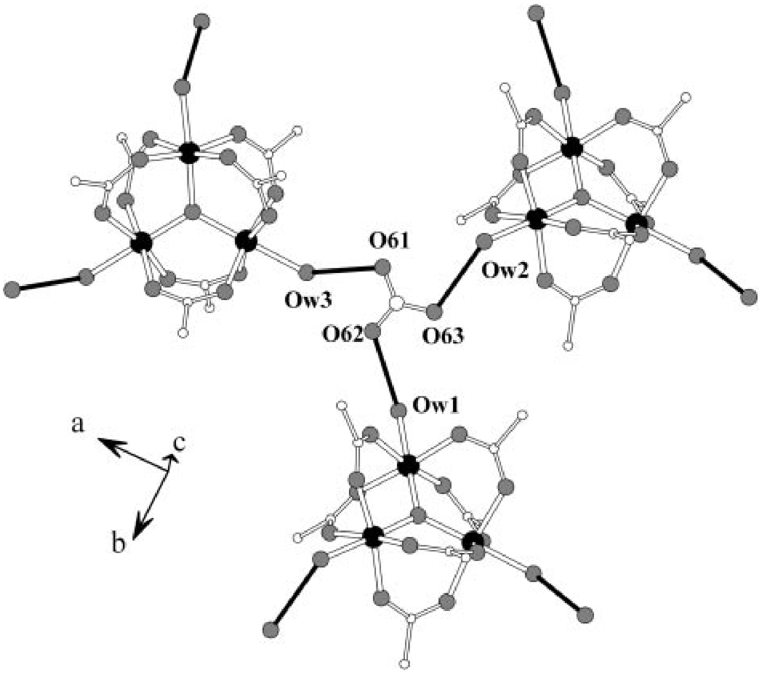

Figure 5. Plot of the 2D polymeric structure of **4** parallel to the *ab* plane. Hydrogen bonds are shown as thick black lines (only the *ipso* carbon atoms of the benzoato ligands are shown). Fe: black circles, O: dark gray, N: large open circles, C: small open circles.

an octahedral environment comprising O donors. The line widths are quite narrow (half width at half maximum $0.20\ \mathrm{mm\,s^{-1}}$), indicating a homogeneous environment around the $\mathrm{Fe^{III}}$ ions. Complex **3** is characterized by a larger value for ΔE_Q than complex **4**, indicating a larger electric field gradient (EFG) for the ferric sites for complex **3**. Inspection of the iron environments for the two compounds suggests that this larger EFG cannot be of geometrical origin; there are no systematic geometrical deviations between **3** and **4** for the ferric octahedra. The larger ΔE_Q for **3** may suggest, however, a larger charge asymmetry imposed by the different nature of the two carboxylates.

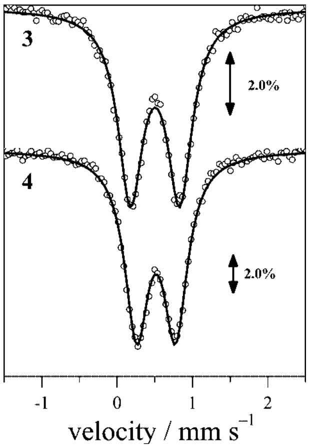

Figure 6. Zero-field Mössbauer spectra from solid powder samples of complexes **3** and **4** at 78 K.

Magnetic Susceptibility Measurements

$\mathrm{Cr^{III}}$ Complexes

The $\chi_M T$ product at 300 K is 4.00 and $3.70\ \mathrm{cm^3\,mol^{-1}\,K}$ for **1** and **2** respectively, appreciably below the value anticipated for three noninteracting $S = 3/2$ spins ($5.61\ \mathrm{cm^3\,mol^{-1}\,K}$), indicative of antiferromagnetic interactions (Figure 7). On cooling, this drops to $0.43\ \mathrm{cm^3\,mol^{-1}\,K}$ (for **1**) and $0.36\ \mathrm{cm^3\,mol^{-1}\,K}$ at 2 K (for **2**) not extrapolating to zero at 0 K, thus suggesting the existence of a paramagnetic impurity and/or a magnetic ground state. The χ_M versus T plots show a gradual increase upon cooling, with a

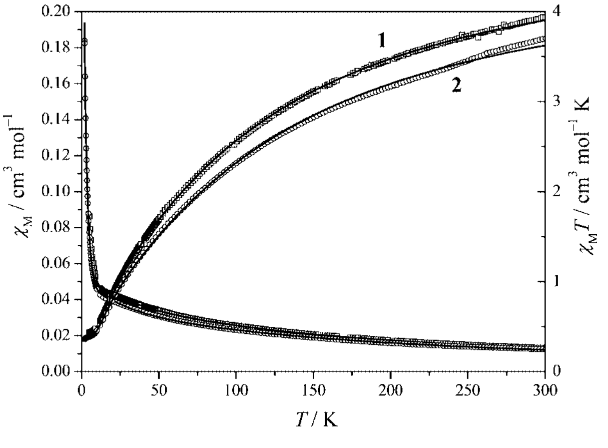

Figure 7. χ_M vs. T and $\chi_M T$ vs. T experimental data for complexes **1** (□) and **2** (○) and theoretical curves based on the Hamiltonian of Equation (4), using the parameters of solutions **1B** and **2B**, respectively.

more abrupt increase below 12 K, probably attributed to a paramagnetic impurity.

To fit the data, an initial model consisting of three equal J values was considered, with the Hamiltonian being [Equation (3)]:

$$\hat{H} = -2J(\hat{\mathbf{S}}_1\hat{\mathbf{S}}_2 + \hat{\mathbf{S}}_2\hat{\mathbf{S}}_3 + \hat{\mathbf{S}}_1\hat{\mathbf{S}}_3) \quad (3)$$

where $S_i = 3/2$.

Assuming a small fraction of paramagnetic impurities, ρ, this model yielded satisfactory solutions with parameters $J = -10.3\ \text{cm}^{-1}$, $g = 1.87$, $\rho = 1.0\%$, and $R = 1.5\times10^{-5}$ for **1** (solution **1A**) and $J = -10.2\ \text{cm}^{-1}$, $g = 1.79$, $\rho = 0.8\%$, and $R = 3.8\times10^{-4}$ for **2** (solution **2A**). On further examining the system, a 2J model was considered, in order to assess the validity of the previous results. The corresponding Hamiltonian was [Equation (4)]:

$$\hat{H} = -2[J(\hat{\mathbf{S}}_1\hat{\mathbf{S}}_2 + \hat{\mathbf{S}}_1\hat{\mathbf{S}}_3) + J'\hat{\mathbf{S}}_2\hat{\mathbf{S}}_3] \quad (4)$$

An examination of the parameter space for this model indicated the existence of two local minima (Figures S1 and S2, Supporting Information). On examining each, two solutions were obtained for complex **1**, with best-fit parameters $J = -10.6\ \text{cm}^{-1}$, $J' = -9.9\ \text{cm}^{-1}$, $g = 1.87$, $\rho = 0.98\%$, and $R = 1.3\times10^{-5}$ (**1B**) and $J = -10.1\ \text{cm}^{-1}$, $J' = -10.9\ \text{cm}^{-1}$, $g = 1.87$, $\rho = 0.98\%$, and $R = 1.3\times10^{-5}$ (**1C**). Similarly, two solutions were obtained for **2**, with best-fit parameters $J = -11.7\ \text{cm}^{-1}$, $J' = -9.6\ \text{cm}^{-1}$, $g = 1.82$, $\rho = 0.62\%$, and $R = 1.4\times10^{-4}$ (**2B**) and $J = -10.2\ \text{cm}^{-1}$, $J' = -12.9\ \text{cm}^{-1}$, $g = 1.82$, $\rho = 0.62\%$, and $R = 1.5\times10^{-4}$ (**2C**).

Solutions **1B**, **1C** and **2B**, **2C** are comparable in quality and only marginally better than solutions **1A** and **2A**, respectively. This small improvement of quality in the fits may stem from the fact that the isosceles model is more adequate, but might also be a result of overparametrization. This is further discussed below (see EPR Spectroscopy).

In order to further examine the validity of these results, the M versus H isotherms of **1** and **2** were measured and compared to the calculated ones, for each one of the solutions. In each case the magnetization isotherms were practically superimposable, and verified the data perfectly. Characteristic plots are shown in Figures S3 and S4 in the Supporting Information.

Fe^{III} Complexes

At 300 K the $\chi_M T$ product is 4.69 cm^{3}mol^{-1}K for complex **3** and 3.67 cm^{3}mol^{-1}K for complex **4**, significantly lower than the theoretically expected value for three noninteracting $S = 5/2$ spins (13.14 cm^{3}mol^{-1}K), indicating antiferromagnetic interactions (Figure 8). Upon cooling, the $\chi_M T$ product decreases without extrapolating to zero at 0 K, which also agrees with the interplay of antiferromagnetic interactions and a magnetic ground state.

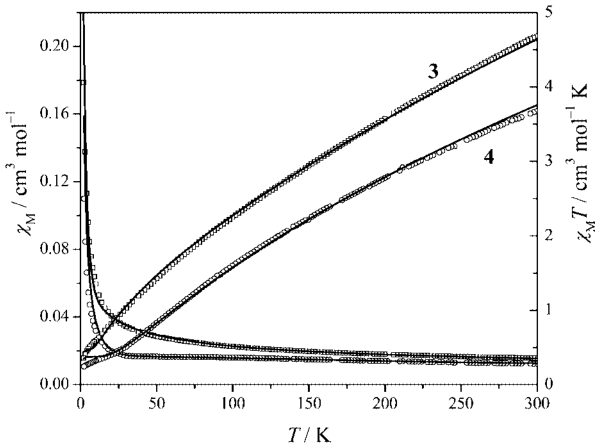

Figure 8. χ_M vs. T and $\chi_M T$ vs. T experimental data for complexes **3** (□) and **4** (○) and theoretical curves based on the Hamiltonian of Equation (4), using the parameters of solutions **3B** and **4C**, respectively.

Initial attempts to simulate the magnetic properties of complex **3** by considering a single J interaction, viewing the complex as an equilateral triangle [Equation (3)], did not yield satisfactory results, so the Hamiltonian of Equation (4) was considered (with $S_i = 5/2$). From the fitting process two solutions of satisfactory quality were obtained, with a small amount of paramagnetic impurity, with their parameters being $J = -27.5\ \text{cm}^{-1}$, $J' = -20.5\ \text{cm}^{-1}$, $\rho = 0.36\%$, $g = 2.0$, and $R = 1.0\times10^{-3}$ (**3B**) and $J = -22.5\ \text{cm}^{-1}$, $J' = -32.6\ \text{cm}^{-1}$, $\rho = 0.35\%$, $g = 2.0$, and $R = 1.1\times10^{-3}$ (**3C**). These two solutions were also located on error contour-plots drawn for various values of J versus J' (Figure S7).

The above-mentioned solutions were further verified by simulations of the M versus H isotherm at 4 K (Figure S7). The experimental data were very well simulated using any set best-fit parameters, which yielded practically superimposable calculated curves.

The behavior of complex **4** could not be accounted for by this model in the low-temperature region, so fits were carried out between 300 and 14 K. These also yielded two solutions, with parameters $J = -34.9\ \text{cm}^{-1}$, $J' = -29.3\ \text{cm}^{-1}$, $\rho = 0$, $g = 2.0$, and $R = 2.7\times10^{-4}$ (**4B**) and $J = -31.0\ \text{cm}^{-1}$, $J' = -38.4\ \text{cm}^{-1}$, $\rho = 0$, $g = 2.0$, and $R = 1.7\times10^{-4}$ (**4C**), which were also located on error contour-plots for various J versus J' values (Table 2) (Figure S8). Below 14 K the experimental curve dropped below the theoretically calculated one. This was also evidenced from the magnetization curve, which at 2.5 is significantly lower than the one theoretically calculated based on the best-fit parameters (Figure S10).

Considering that exchange couplings are primarily mediated through the oxide ions,[32] the J values for the Fe^{III} complexes are very close to those derived by applying the formula proposed by Weihe and Güdel[33,34] using the Fe–O distances and the Fe–O–Fe bridging angles. Although for dinuclear Cr^{III} compounds the exchange coupling depends on the same parameters (distances and bringing angles),[35] an analogous magnetostructural correlation scheme has not

Table 2. Exchange-coupling constants derived for complexes **1**–**4**.

Best-fit solution	J (cm^{-1})	J' (cm^{-1})	J_{av}[a] (cm^{-1})	g[b]
1A	–10.3			1.87
1B	–10.6	–9.9	–10.4	1.87
1C	–10.1	–10.9	–10.4	1.87
2A	–10.2			1.79
2B	–11.7	–9.6	–11.0	1.82
2C	–10.2	–12.9	–11.1	1.82
3B	–27.5	–20.5	–25.2	**2.00**
3C	–22.5	–32.6	–25.9	**2.00**
4B	–34.9	–29.3	–33.0	**2.00**
4C	–31.0	–38.4	–33.5	**2.00**

[a] $J_{av} = (2J + J')/3$. [b] Values in bold were fixed during the fitting process.

yet been obtained for Cr^{III} compounds[36] with nuclearity three and higher. The values obtained for the exchange parameters (J, J') are very close to the corresponding values from similar trinuclear oxobridged Cr^{III} and Fe^{III} compounds.[3]

The ligands seem to have no discernible influence on the magnetic properties of the Cr^{III}-based complexes. On the contrary, in the case of Fe^{III}-based complexes the J values are larger in the case of the benzoate ligand (**4**), as has also been observed in another series of trinuclear iron(III) carboxylate complexes.[37]

Although the number of examples presented herein is hardly sufficient to establish a valid correlation, we may still assume that there is some influence of the carboxylato ligand's electronic parameters on the magnitude of the exchange couplings. This influence should be secondary to that induced by the variation of structural parameters like M···M distances and M–O–M angles, but is probably not negligible. Such an influence has also been observed by Mössbauer spectroscopy, which reveals a larger (ca. 25%) quadrupole splitting for the ferric sites in **3** despite having very similar geometrical environments to the ferric sites in **4**.

In assessing the metal influence on the magnetic properties of the complexes, we first observe that couplings are stronger in iron(III) complexes than in their chromium(III) counterparts, by a factor of about 3. Secondly, we observe that, as in the case of "basic iron(III) carboxylates", "basic chromium(III) carboxylates" present two best-fit solutions of their magnetic susceptibility data within the isosceles model, one with $J > J'$ and one with $J < J'$. However, an important difference is that in the case of chromium(III) complexes these solutions are comparable in quality with the solution derived from the equilateral model ($J = J'$), whereas in the case of iron(III) complexes the latter model fails to satisfactorily reproduce the experimental data. Therefore, although the equilateral model may be insufficient to describe "basic chromium(III) carboxylates", other techniques (like EPR) are necessary to unambiguously prove this.

Solid-State NMR

Solid-state NMR experiments in magnetic molecular clusters of transition-metal ions probe the magnetic excitations in the electronic spin system of the cluster. In particular, at low temperatures, T_1 spin-lattice relaxation measurements are quite sensitive to the low-lying energy levels of the system. The ^{1}H NMR spin-lattice relaxation time T_1 was measured at an applied magnetic field $H = 4.7$ T, between room and liquid-helium temperatures. The relaxation rate $1/T_1$ as a function of temperature is shown in Figure 9. At high temperatures the relaxation rate exhibits a weak temperature dependence, while below around 80 K an activated-type dependence is observed. The temperature dependence of $1/T_1$ measured for **1** is analogous to a previously studied trinuclear Cr^{III} complex[26] and has a behavior that has been frequently encountered in previous ^{1}H NMR studies of molecular clusters that include transition-metal ions with low S values, for example $S = 1/2$, $3/2$.[38] The NMR $1/T_1$ relaxation data in clusters including metal ions with high S values, such as $S = 5/2$, frequently exhibit a pronounced $1/T_1$ maximum at temperatures of the order of the exchange frequency J.[39,40] The absence of a maximum in clusters with metal ions having low S values has not been adequately explained so far and is currently under investigation.

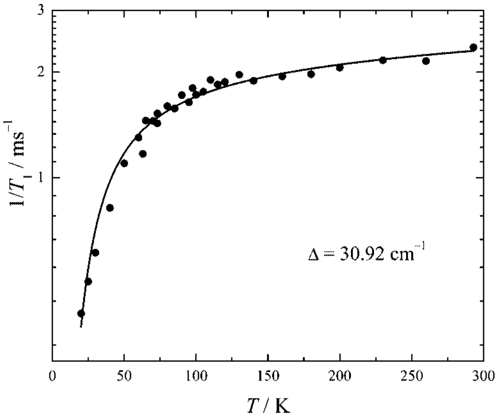

Figure 9. The relaxation rate $1/T_1$ as a function of temperature for **1**.

Using a two-level system and an Orbach-type activation process for the electronic excitation, we have been able to fit the experimental data considering an energy gap consistent with that obtained from the susceptibility data. In this model the NMR relaxation is caused by the local field fluctuations originating from the magnetic excitations from the ground state to the excited state, separated by the energy difference Δ. Assuming that the Cr^{III} spin system remains in the ground state for an average time τ_0 and in the excited state for a lifetime τ_1, during which an effective transverse local field $h_\perp$ appears at the nuclear site, the relaxation rate is expressed as [Equation (5)]:[41]

$$\frac{1}{T_1} = (\gamma_N h_\perp)^2 \frac{\tau_1 \tau_0}{(\tau_1 + \tau_0)^2} \frac{\tau}{(\omega_N \tau)^2 + 1} \tag{5}$$

where

$$\frac{1}{\tau} = \frac{1}{\tau_0} + \frac{1}{\tau_1}$$

γ_N is the proton gyromagnetic ratio, and ω_N is the Larmor angular frequency.

This model has been frequently employed for the nuclear magnetic relaxation in paramagnets.[38,42,43] For the excitation $1/\tau_0$, we may consider the sum of two processes [Equation (6)]:[44]

$$\frac{1}{\tau_0} = A_0 \coth(\frac{g\mu_B H}{2k_B T}) + B_0 \exp(-\frac{\Delta}{k_B T}) \tag{6}$$

The first term is a direct-type process, generally applicable at low temperatures, and the second term is an activation process of the Orbach type because of the presence of the energy level spacing Δ and is generally applicable at higher temperatures.

For the lifetime τ_1 we consider a temperature-independent term [Equation (7)]:

$$1/\tau_1 = C_1 \tag{7}$$

Setting ν_N = 200.1 MHz (H = 4.7 T), and using Equations (6) and (7), the experimental NMR points are fitted to Equation (5), shown as a solid line in Figure 13. The influence of the first term in Equation (6), the direct process, is quite small in the experimental determination of Δ. We observe that the line describes the overall experimental features rather well. The value of Δ determined by the fitting is Δ = 30.92 cm^{-1}. According to the analysis of the magnetic susceptibility measurements for Cr^{III} compounds presented in the previous paragraph, the ground state has S_T = 1/2 (T for total) and the first excited state has S_T = 3/2. For an equilateral exchange interaction model, which is the case (to a good approximation) for the Cr^{III} compounds, Δ = 3J[4] ≈ 30 cm^{-1} (for J ≈ 10 cm^{-1}). Both values for the first excited multiple determined by the analysis of the susceptibility and NMR measurements are in good agreement.

EPR Spectroscopy

EPR spectroscopy has been proven to be very useful in determining the magnetic properties of the ground state of trinuclear complexes.[2,4,5,17–23]

Cr^{III} Complexes

X-band EPR spectra from powder samples of **1** and **2** recorded at 4.2 K are shown in Figure 10. Both samples give rise to strong signals comprising an absorption peak at g ≈ 1.97–1.98 and broad features at higher magnetic fields (Figures 10, left and right). The magnetic susceptibility data indicate an S_T = 1/2 ground state for complexes **1** and **2**. Indeed, the signals of Figure 10 are consistent with an isolated S_T = 1/2 state. In coupled trimers, a relatively large anisotropy in the g tensor for the S_T = 1/2 ground state with a $g_\perp$ value significantly smaller than 2 is usually observed. This anisotropy is the result of antisymmetric exchange interaction [Equation (8)]:

$$\hat{H}_{AE} = \mathbf{d}(\hat{\mathbf{S}}_1 \times \hat{\mathbf{S}}_2 + \hat{\mathbf{S}}_2 \times \hat{\mathbf{S}}_3 + \hat{\mathbf{S}}_3 \times \hat{\mathbf{S}}_1) \tag{8}$$

In the framework of Hamiltonian (8), $g_\parallel \approx g_0$, where g_0 is the g value for the Cr^{III} metal ion. $g_\perp$ depends critically on the relationship between d and ΔE, where ΔE is the energy difference between the two lowest S_T = 1/2 states. In the case of well-isolated S_T = 1/2 doublets with respect to the higher S = 3/2 states and small d values, the dependence

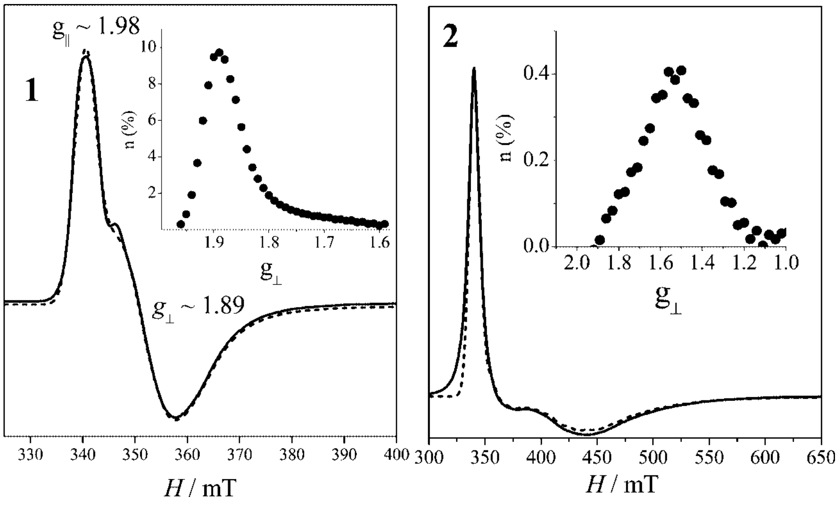

Figure 10. X-band EPR spectra in the high-field region from powdered samples from compounds **1** (left) and **2** (right) at 4.2 K. Dashed lines represent theoretical simulations as described in the text. Inset: Distribution of subspectra used to generate the simulations as described in the text. EPR conditions: microwave power 2.0 mW, mod. amplitude, 1.0 mT (left), 0.4 mT (right), microwave frequency 9.42 GHz.

of $g_\perp$ on these parameters is given analytically through the relationship [Equation (9)]:[19]

$$g_\perp = g_{0\perp}\left[1 - \frac{D^2}{\Delta E^2 - (h\nu)^2}\right]^{1/2} \tag{9}$$

ΔE stands for the separation of the lowest $S = 1/2$ doublets and is given by the relationship [Equation (10)]:

$$\Delta E = (\sigma^2 + D^2)^{1/2} \tag{10}$$

where $D = 4\sqrt{3}d$, and $\sigma = 4|J - J'|$.

From this model the characteristics of the spectra shown in Figure 10 can be understood. The absorption peak observed at $g \approx 1.97$–1.98 is attributed to the $g_\parallel$ component, whereas the broad derivative feature corresponds to $g_\perp$. Recently[26] we have observed similar EPR spectra in a Cr^{III} complex similar to **2**. In order to reproduce the line shape of the spectra we follow the same procedure as in that case. Namely, we calculate a large number of axial spectra with $g_\parallel \approx 1.97$–1.98 and with smaller $g_\perp$ values, and then by a fitting routine we determine the distribution of the subspectra that reproduce the experimental one. The resulting simulations together with the distributions of the subspectra are shown in the insets in Figure 10.

In both cases the distribution profiles exhibit a maximum at certain g values (1.90 for **1** and 1.53 for **2**). These values are considered as the $g_\perp$ for the $S = 1/2$ ground states. The crystal structure at room temperature revealed an isosceles configuration for **1** and an almost equilateral for **2**. The magnetic susceptibility measurements gave satisfactory results either with an equilateral ($J = J'$) or with an isosceles model ($J \neq J'$). An $S = 1/2$ EPR signal with an axial character cannot arise from a trinuclear system with $J = J'$, because in this case the transition probability corresponding to the $g_\parallel$ component vanishes.[5,13,18]

From the dependence of $g_\perp$ on the antisymmetric exchange parameter $|\mathbf{d}|$, the magnitude of the latter can be determined. For this, knowledge of $g_{0\perp}$ and ΔE is also required. For Cr^{III} ($S = 3/2$) the intrinsic $\mathbf{g_0}$ tensor is slightly anisotropic with values $g_{0\parallel}$ and $g_{0\perp}$ smaller than 2 and in the 1.98–1.93 range. For the coupled system the $g_\parallel$ parameter does not depend on $|\mathbf{d}|$, therefore we can safely assume that $g_\parallel \equiv g_{0\parallel}$. For the perpendicular component we assume that $g_{0\perp}$ lies in the 1.98–1.93 region.

Although for the description of the magnetic susceptibility data we did not take into account the antisymmetric term, the determined values for J and J' can be used in order to estimate the separation, ΔE of the two lowest $S = 1/2$ states. We consider also that their average value $J_{av} = (2J + J')/3$ is valid as it satisfactorily reproduces the temperature dependence of the magnetic susceptibility. From Equation (9) and the given values for ΔE we determine the antisymmetric exchange parameter $|\mathbf{d}|$ for the two solutions (**1B**, **1C** and **2B**, **2C**). From these values we estimate that $|\mathbf{d}| \approx 0.10$ cm^{-1} for **1** and $|\mathbf{d}| \approx 1.1$ cm^{-1} for **2**. These values fall in the range reported for other carboxylato-bridged trinuclear complexes.[19] $|\mathbf{d}|$ is significantly larger for compound **2**, suggesting that the nature of the carboxylato-bridging ligands affects the magnitude of the antisymmetric exchange interaction.

From Equation (10) we find that $\sigma \approx 3$ cm^{-1} for **1** and $\sigma \approx 6$ cm^{-1} for **2**. This parameter depicts the splitting of the $S = 1/2$ doublets, which is due to the nonequivalence of the isotropic exchange parameters. We observe that incorporation of antisymmetric exchange through Equation (10) leads to a slightly smaller σ compared with the one derived from a purely isotropic exchange Hamiltonian, which was considered in the analysis of the magnetic susceptibility data. From the relationship $\sigma = 4|J - J'|$ we see that the actual J and J' values should be slightly different from those derived from the analysis of the magnetic susceptibility data. This difference is too small to be discernible in the analysis of the temperature dependence of the magnetic susceptibility. Moreover, the magnitude of the antisymmetric exchange parameter $|\mathbf{d}|$ derived from the analysis of the EPR data is not expected to affect this analysis.

The parameter σ can be taken as a measure for the lowering of the symmetry because for an equilateral triangle $\sigma = 0$. For compound **1** a non-zero value for σ could be anticipated, as the room temperature crystal structure already reveals an isosceles configuration. On the contrary, compound **2** has an equilateral configuration at room temperature. Therefore the finite value of σ for this compound (even larger than compound **1**) indicates a lowering of symmetry at low temperatures. The lowering of symmetry is one of the properties of trinuclear complexes that have been the subject of extensive studies during the last few decades, and from this point of view compound **2** belongs to this family of clusters.

The distribution of $g_\perp$ values required to reproduce the EPR spectra of Figure 10 is noteworthy. The distribution is more pronounced for compound **2**. From Equation (9) we observe that $g_\perp$ is extremely sensitive on the ratio $d/\Delta E$. A relatively small distribution on this parameter would lead to a large distribution of the g values, resulting in a severely distorted axial EPR spectrum. This distribution may arise from structural inhomogeneities, resulting for instance from partial solvent loss. Alternatively, this behavior may be connected with the lowering of the symmetry discussed above. We note that, as ΔE depends on σ, a small distribution of the isotropic exchange constants would have a prominent effect. These constants are expected to depend on the geometrical characteristics of the clusters. It is probable, therefore, that upon cooling a multitude of geometric configurations are trapped, giving rise to slightly different sets of J values, resulting eventually in a variety of σ values. This effect would be more pronounced for compound **2** on going from the equilateral to isosceles configuration upon decrease of temperature.

As the temperature increases, new signals emerge in the lower-field region of the spectra, as shown in Figure 11. The temperature dependence of these signals indicates that they arise from excited states of a paramagnetic system. This is strong evidence against an assignment of these signals to mononuclear Cr^{III} ($S = 3/2$) impurities.[46] On the other hand, they can be very well attributed to excited states with

$S > 1/2$ of the trimeric units, which are gradually populated as the temperature increases. The energy level with $S_T = 3/2$ is the most probable to generate these signals, because it is the first excited state with $S > 1/2$ for the system.

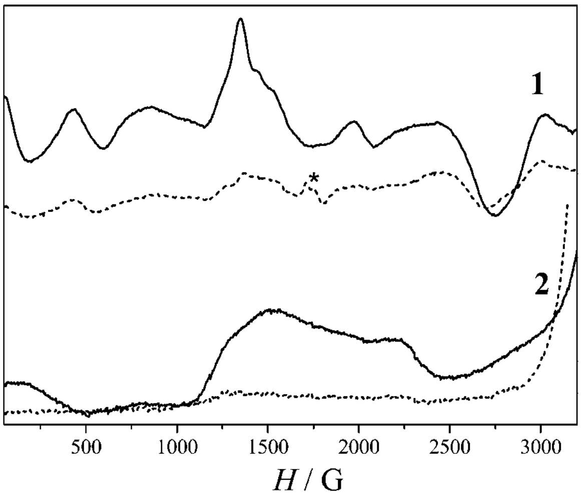

Figure 11. The low magnetic field region of EPR spectra from polycrystalline samples of **1** and **2** at 4.2 K (dotted lines) and 19 K (continuous lines). The asterisk * denotes a weak signal, which is attributed to impurities. EPR conditions: microwave power 2.0 mW, mod. amplitude 1.0 mT, microwave frequency 9.42 GHz.

For an equilateral triangle one has four states with $S_T = 3/2$ with the same energy. For $J \neq J'$ these states differ in energy leading to four separate quartets. Moreover, further splitting may be induced from non-Heisenberg interactions such as single-ion zero-field splitting, dipolar, and antisymmetric exchange. The analysis of the $S_T = 1/2$ signals from the ground state indicates that the magnitude of these interactions is too small to be discernible in the bulk magnetic susceptibility measurements; however they induce very complicated EPR spectra. As is clearly shown in Figure 11, the two complexes differ not only in the EPR spectra obtained from the $S_T = 1/2$ ground state, but also in the EPR spectra from the excited states.

Fe^{III} Complexes

The EPR spectrum recorded at 4.2 K from a polycrystalline sample of compound **3** is shown in Figure 12. Although the analysis of magnetic susceptibility measurements reveals that the ground state for compound **3** has $S_T = 1/2$, as in the case of compounds **1** and **2**, the EPR spectrum for this compound is different. Specifically, a very intense signal is observed at $g \approx 2.0$ and a number of weaker signals are recorded at lower values of the magnetic field. The signal recorded at $g = 2.0$ has a width of about 600 G, and comprises an absorption feature at $g \approx 2.18$, a derivative at $g \approx 1.98$, and a valley at 1.86. These signals are not explained by considering an isolated trinuclear complex as in the case of Cr^{III}-based **1** and **2** complexes. Recently, we have observed similar EPR spectra from powdered samples of another trinuclear complex and for their interpretation we suggested inter-trimer interactions leading to weakly coupled dimers of trinuclear units.[31] The crystal structure of **3** reveals intermolecular interactions leading to the formation of dimers of trinuclear centers. In order to reproduce the spectra we have employed the same model as in ref.[31] involving two weakly interacting $S_1 = S_2 = 1/2$ species in the framework of the spin Hamiltonian [Equation (11)]:[20]

$$\hat{H} = \hat{\mathbf{S}}_1\tilde{\mathbf{J}}_{12}\hat{\mathbf{S}}_2 + \hat{\mathbf{S}}_1\mathbf{g}_1\mathbf{B} + \hat{\mathbf{S}}_2\mathbf{g}_2\mathbf{B} \qquad (11)$$

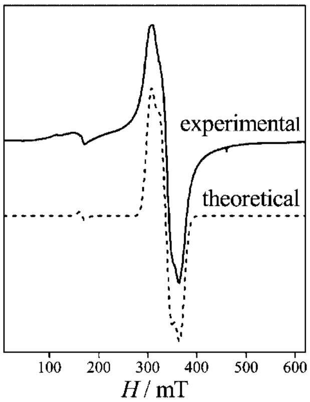

Figure 12. Experimental (solid) and theoretical (dotted) perpendicular-mode X-band EPR spectra from a powdered sample of **3** at 4.2 K. The simulation is obtained as described in the text using an intrinsic line width of 7 mT. EPR conditions: microwave power 2.0 mW, mod. amplitude 0.4 mT, microwave frequency 9.42 GHz.

The exchange interaction is represented by an anisotropic diagonal tensor $\tilde{\mathbf{J}}$. The distance between the trinuclear complexes in a dimer unit is relatively large and the isotropic exchange interaction is expected to be negligible. We find that the spectra are well reproduced for $\mathbf{J}$ = [0.04, 0.00, –0.04] cm^{-1} with $g_1 = g_2 = 2.0$. The interaction of Equation (11) leads to a four-energy-level system.

Within this, manifold "half-field" transitions are expected at $g \approx 4.0$.[47] Indeed, such signals are observed in the EPR spectra of Figure 12. It could be argued that the signals in the $g \approx 4$ region arise from high-spin Fe^{III} impurities which exhibit derivative signals at $g \approx 4.3$. In order to deduce whether the signals in the $g \approx 4.0$ region belong to the exchange coupled system of Equation (11) or arise from Fe^{III} impurities, we have performed EPR spectroscopy in parallel mode (Figure 13). For a high-spin Fe^{III} impurity with a zero-field splitting term $|D| \approx 1–2\ cm^{-1}$, the $g \approx 4.3$ component has no contribution in parallel mode, as it arises from a Kramers doublet. The "half-field" transitions of a system described by Equation (11) involve non-Kramers doublets and the transition probability in parallel mode is finite. The existence of a signal at $g \approx 4.0$ in the parallel mode spectrum provides further evidence for an anisotropic exchange interaction between two neighboring $S = 1/2$ trimers.

The spectra are reproduced assuming isotropic $\mathbf{g}_i$ tensors with $g = 2.00$. From this point of view, complex **3** does not exhibit anisotropic g tensors for the ground $S = 1/2$ state, unlike the Cr analogue complex **1**, for which anisotropic $S = 1/2$ signals are observed (Figure 10). Therefore, there is no indication for antisymmetric exchange in the case of **3**.

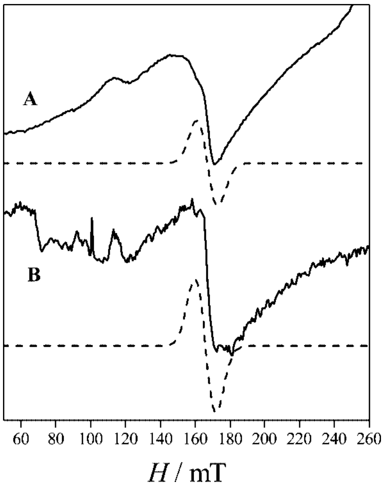

Figure 13. Experimental (solid) and theoretical (dotted) dual-mode X-band EPR spectra from powdered samples of **3** at 4.2 K. A: perpendicular mode; B: parallel mode. Simulations are obtained as described in the text. EPR conditions: A, as in Figure 11; B, microwave power 54 mW, mod. amplitude 0.4 mT, microwave frequency 9.36 GHz.

The anisotropic exchange interaction is mainly of dipolar origin. In the present case, the spin in each trimer delocalizes in three Fe^{III} ions and the size of the triangles is of the same order of magnitude with the distance between the species. In such a case a point-dipole model is not a good approximation. We have observed similar EPR spectra from powdered samples of another trinuclear complex.[31]

Powdered samples from **4** gave rise to complicated EPR spectra at liquid helium temperatures extending several hundreds of mT. We have studied many samples exhibiting identical Mössbauer and IR spectra but each time their EPR spectra showed variations. A representative spectrum is shown in Figure S13. The X-band EPR spectra cannot be interpreted assuming isolated $S = 1/2$ species. The simplified model for intermolecular interactions, adopted in the case of **3**, does not apply to **4** either. Moreover, we note that the magnetic susceptibility data for liquid helium temperatures exhibited significant deviation from the isotropic exchange Hamiltonian [Equations (3) and (4)]. Therefore, it appears that more complicated magnetic interactions have to be taken into account in order to appropriately describe the low-temperature magnetic behavior of **4**.

Conclusions

Structural, magnetic, and EPR spectroscopic studies have been carried out on two basic chromium(III) and two basic iron(III) carboxylates. In addition, solid-state ^1H NMR studies have been carried out on **1** and ^{57}Fe Mössbauer studies have been carried out on the ferric complexes **3** and **4**. This allowed us to examine the influence of ligand and metal variation on structural, magnetic, and spectroscopic properties.

From a structural viewpoint benzilato ligands induce a nearly isosceles geometry in **1** and **3**, whereas benzoato ligands induce a nearly equilateral geometry. However, these geometric characteristics are not reflected in the "magnetic symmetry" of the complexes; the magnetic susceptibility data of the chromium(III) complexes can be well described both by the equilateral or isosceles model, whereas those of the iron(III) complexes demand the use of the isosceles model. In the case of the isosceles model, two best-fit solutions are obtained for all complexes. Solid-state ^1H NMR studies on **1** reveal that the first excited state is well separated from the ground state and quantitatively confirm the magnetic susceptibility results.

Further information regarding the low-lying spin states of the trimers was obtained by X-band EPR spectroscopy. For **1** and **2** the EPR results favor the isosceles model at least at liquid helium temperatures and confirm the $S_T = 1/2$ ground state. In addition, in **1** and **2** the presence of antisymmetric exchange was revealed along with a distribution of the exchange parameters.

Concerning the iron(III) complexes, the EPR spectrum of **3** is influenced by intermolecular interactions of dipolar origin, whereas that of **4** is too complicated to be analyzed in detail. It is however concluded that antisymmetric exchange is not so important in **3**.

Another point of interest concerns the ligand-induced electronic effects on various magnetic and spectroscopic properties. In particular, it was observed that: (i) isotropic exchange couplings are stronger within benzoato complexes (**2**/**4**) than within benzilato complexes (**1**/**3**), (ii) the electric field gradient is larger for the ferric sites of the "basic iron(III) benzilate" (**3**) than for the sites of the "basic iron(III) benzoate" (**4**), and (iii) the magnitude of the antisymmetric exchange parameter **d** is about 10 times larger for **2** than for **1**.

These differences gain importance with the close structural resemblance of **1**/**2** and **3**/**4**, which does not allow for their simple geometric interpretation. Rather, we assume that electronic factors affect the exchange couplings (isotropic and antisymmetric) and EFG, although this point requires more elaborate studies. Weak intermolecular, metal-dependent interactions may complicate the analysis of the properties of the trinuclear units.

Experimental Section

Compound Preparations: All manipulations were performed under aerobic conditions using materials as received (Aldrich Co). All chemicals and solvents were of reagent grade.

$[Cr_3(\mu_3\text{-}O)\{O_2C(OH)Ph_2\}_6(H_2O)_3](NO_3)\cdot 2H_2O\cdot 3Me_2CO$ ($1\cdot 2H_2O\cdot 3Me_2CO$): Solid benzilic acid (0.233 g, 1.01 mmol) was added to a refluxing green-purple solution of $Cr(NO_3)_3\cdot 9H_2O$ (0.204 g, 0.51 mmol) in Me_2CO (15 mL). The reflux continued for 3 days, giving a green solution, which was layered with a mixture of Et_2O/*n*-hexane (1:1 v/v %) to afford X-ray-quality green crystals of **1**. The crystals were collected by filtration, and dried in vacuo. (Yield: 0.34 g, ca. 70%.) The resulting powder was analyzed as solvent-free. $C_{84}H_{72}Cr_3NO_{25}$ (1651.47): calcd. C 61.09, H 4.39, N 0.85; found C 60.15, H 4.32, N 0.80. Selected IR data: 3614 [$\nu(OH)_{free}$], 1636 [$\nu_{as}(COO)$], 1415 [$\nu_s(COO)$], 600 [$\nu_{as}(Cr_3O)$] cm^{-1}.

$[Cr_3(\mu_3\text{-}O)(O_2CPh)_6(H_2O)_3](NO_3)\cdot1.9MeCN\cdot0.5H_2O$ ($2\cdot1.9MeCN\cdot0.5H_2O$): Solid sodium benzoate (0.373 g, 2.58 mmol) was added to a refluxing green-purple solution of $Cr(NO_3)_3\cdot9H_2O$ (0.517 g, 1.29 mmol) in MeCN (15 mL). The reflux continued for 2 h, giving a green solution, which upon slow evaporation afforded X-ray-quality green crystals of **2**. (Yield: 0.34 g, ca. 70%.) The crystals of **2** were collected by filtration and dried in vacuo. The resulting powder was analyzed as solvent-free. $C_{42}H_{36}Cr_3NO_{19}$ (1014.73): calcd. C 49.71, H 3.58, N 1.38; found C 48.90, H 3.44, N 1.29. Selected IR data: 1574 [ν_{as}(COO)], 1421 [ν_s(COO)], 620 [$\nu_{as}(Cr_3O)$] cm^{-1}.

$[Fe_3(\mu_3\text{-}O)\{O_2C(OH)Ph_2\}_6(H_2O)_3](NO_3)\cdot5.69H_2O$ ($3\cdot5.69H_2O$): Solid benzilic acid (0.228 g, 1.00 mmol) was added to a refluxing solution of $Fe(NO_3)_3\cdot9H_2O$ (0.202 g, 0.50 mmol) in CH_2Cl_2 (20 mL). The color of the solution gradually turned from red to orange and the reflux continued for 2 h. The $NaNO_3$ that precipitated was filtered off and the orange filtrate was layered with *n*-hexane (1:1 v/v %). Orange crystals of **3** suitable for X-ray structure analysis were formed after one week. (Yield: 0.34 g, ca. 70%.) The crystals of **3** were collected by filtration and dried in vacuo. The resulting powder was analyzed as solvent-free. $C_{84}H_{72}Fe_3NO_{25}$ (1663.03): calcd. C 60.67, H 4.36, N 0.84; found C 59.86, H 4.28, N 0.80. Selected IR data: 3603 [$\nu(OH)_{free}$], 1612 [ν_{as}(COO)], 1406 [ν_s(COO)], 598 [$\nu_{as}(Fe_3O)$]cm^{-1}.

$[Fe_3(\mu_3\text{-}O)(O_2CPh)_6(H_2O)_3](NO_3)\cdot3MeCN$ ($4\cdot3MeCN$): Solid sodium benzoate (0.144 g, 1.00 mmol) was added to a refluxing solution of $Fe(NO_3)_3\cdot9H_2O$ (0.202 g, 0.50 mmol) in MeCN (20 mL). The color of the solution gradually turned from red to orange and the reflux continued for 24 h. A white precipitate was filtered off and identified as $NaNO_3$ by FTIR spectroscopy. The orange filtrate was left for slow evaporation and after ca. 1 week, X-ray-quality orange crystals of **4** were formed. (Yield: 0.34 g, ca. 70%.) The crystals of **4** were collected by filtration and dried in vacuo. The resulting powder was analyzed as solvent-free. $C_{42}H_{36}Fe_3NO_{19}$ (1026.28): calcd. C 49.15, H 3.54, N 1.36; found C 48.30, H 3.22, N 1.27. Selected IR data: 1562 [ν_{as}(COO)], 1410 [ν_s(COO)], 573 [$\nu_{as}(Fe_3O)$] cm^{-1}.

Physical Measurements: Elemental analyses for carbon, hydrogen, and nitrogen were performed on a Perkin–Elmer 2400/*II* automatic analyzer. Infrared spectra were recorded as KBr pellets in the range 4000–500 cm^{-1} with a Bruker Equinox 55/S FTIR spectrophotometer. EPR spectra were recorded with a Bruker ER 200D-SRC X-band spectrometer equipped with an Oxford ESR 9 cryostat in the 4.2–300 K temperature range, an NMR Gaussmeter, an Anritsu frequency counter, and a DM Bruker cavity. Simulations of the EPR spectra were done with home-written routines or software provided to us by Prof. Mike Hendrich, Dept. of Chemistry, Carnegie Mellon University, Pittsburgh, USA. Variable-temperature magnetic susceptibility measurements were carried out with polycrystalline samples of **1**–**4** in the 2.0–300 K temperature range using a Quantum Design MPMS SQUID susceptometer under magnetic fields of 0.1 T (for **1**, **2**) and 1.5 T (for **3**, **4**). Isothermal magnetization measurements were carried out over the 0–5 T magnetic field range. Diamagnetic corrections for the complexes were estimated from Pascal's constants. The calculation of the magnetic susceptibility was accomplished by analytical calculation of the energy levels associated with the spin Hamiltonian using Kambe's spin-coupling approach. Subsequent implementation of the van Vleck equation was done using a home-written routine. For the case of the equilateral model, an analytical expression can also be used.[48] Minimization was carried out with an adapted version of MINUIT.[49] The error factor R is defined as $R = \sum(\chi_{exp} - \chi_{calc})^2/N\chi^2_{exp}$, where N is the number of experimental points. Magnetization M versus applied magnetic field H isotherms were calculated from the best-fit parameters using MAGPACK.[50] Mössbauer spectra for **3** and **4** were recorded with a constant acceleration spectrometer using a ^{57}Co (Rh) source at room temperature and a variable-temperature Oxford cryostat. The spectra were analyzed with home-written routines. Variable-temperature ^1H-pulsed NMR experiments for **1** were performed at 4.7 T using a Bruker MSL200 spectrometer operating at 200.145 MHz. An Oxford 1200 CF continuous flow cryostat was employed for measurements in the range 5–300 K. T_1 spin-lattice relaxation times were measured using the standard spin-echo pulse sequence combined with the saturation recovery method.[51]

X-ray Structure Determination: Green prismatic crystals of **1** ($0.25\times0.35\times0.65$ mm) and **2** ($0.20\times0.30\times0.65$ mm), and orange prismatic crystals of **3** ($0.10\times0.25\times0.50$ mm) and **4** ($0.18\times0.28\times0.50$ mm) were mounted in capillaries with drops of mother liquid. Diffraction measurements were made on a Crystal Logic Dual Goniometer diffractometer using graphite-monochromated Mo-K_α radiation. Important crystal data and parameters for data collection are reported in Table 3. Unit cell dimensions were determined and refined by using the angular settings of 25 automatically centered reflections in the range $11° < 2\theta < 23°$. Intensity data were recorded using a θ–2θ scan. Three standard reflections monitored every 97 reflections showed less than 3% intensity fluctuation and no decay. Lorentz, polarization, and psi-scan absorption corrections (for **2** and **3** only) were applied using Crystal Logic software. The structures were solved by direct methods using SHELXS-86[52] and refined by full-matrix least-squares techniques on F^2 with SHELXL-97.[53] In all cases, the crystals had poor diffraction ability (despite their sufficient size) and the data were collected in increasing 2θ shells, and in each case the data collection was terminated when about 50% of the collected shell data were unobserved. Nevertheless, the quality of the collected data was adequate to establish the structure of the complexes. Further experimental crystallographic details for **1**: $2\theta_{max} = 43°$, scan speed $1.3°\,min^{-1}$; scan range 2.0 + $\alpha_{1\alpha2}$ separation; reflections collected/unique/used, 11108/10817 [R_{int} = 0.0394]/10817; 1200 parameters refined; $(\Delta/\sigma)_{max} = 0.011$; $(\Delta\rho)_{max}/(\Delta\rho)_{min}$ = 0.811/–0.352 $e\,Å^{-3}$; R/R_w (for all data), 0.0813/0.1769. All non-hydrogen atoms were refined anisotropically. Hydrogen atoms on the phenyl rings were introduced at calculated positions as riding on bonded atoms; those on the hydroxide and coordinated water molecules were located by difference maps and were refined isotropically. No H atoms for the solvate molecules were included in the refinement. Further experimental crystallographic details for **2**: $2\theta_{max} = 45°$, scan speed $2.5°\,min^{-1}$; scan range 1.7 + $\alpha_{1\alpha2}$ separation; reflections collected/unique/used, 6522/6163 [R_{int} = 0.0255]/6163; 667 parameters refined; $(\Delta/\sigma)_{max} = 0.019$; $(\Delta\rho)_{max}/(\Delta\rho)_{min}$ = 0.762/–0.625 $e\,Å^{-3}$; R/R_w (for all data), 0.0836/0.2175. All non-hydrogen atoms were refined anisotropically, except those of the solvate molecules, which were refined isotropically. Hydrogen atoms on the phenyl rings were introduced at calculated positions as riding on bonded atoms; those of the coordinated water molecules were located by difference maps and were refined isotropically. Further experimental crystallographic details for **3**: $2\theta_{max} = 42.1°$, scan speed $1°\,min^{-1}$; scan range 1.75 + $\alpha_{1\alpha2}$ separation; reflections collected/unique/used, 10064/9849 [R_{int} = 0.0421]/9849; 1080 parameters refined; $(\Delta/\sigma)_{max}$ = 0.001; $(\Delta\rho)_{max}/(\Delta\rho)_{min}$ = 0.687/–0.424 $e\,Å^{-3}$; R/R_w (for all data), 0.1449/0.2373. All non-hydrogen atoms were refined anisotropically, except those of some solvate water molecules that were found to be disordered and were refined isotropically with occupation factors summing one. Hydrogen atoms on the phenyl rings were introduced at calculated positions as riding on bonded atoms; the rest

Table 3. Crystallographic data for complexes **1**–**4**.

	1·$2H_2O$·$3Me_2CO$	**2**·1.9MeCN·$0.5H_2O$	**3**·$5.69H_2O$	**4**·3MeCN
Formula	$C_{93}H_{94}Cr_3NO_{30}$	$C_{45.8}H_{42.7}Cr_3N_{2.9}O_{19.5}$	$C_{84}H_{83.38}Fe_3NO_{30.69}$	$C_{48}H_{45}Fe_3N_4O_{19}$
Formula mass	1861.69	1101.73	1765.49	1149.43
Space group	$P2_1/n$	$P\bar{1}$	$C2/c$	$P2_1/a$
a [Å]	13.647(6)	11.433(7)	32.52(2)	21.33(2)
b [Å]	23.54(1)	11.972(8)	17.02(1)	11.37(1)
c [Å]	29.52(1)	21.76(1)	35.44(3)	22.40(2)
α [°]		84.20(2)		
β [°]	90.47(2)	87.47(2)	106.49(2)	95.42(4)
γ [°]		64.36(2)		
V [Å^3]	9481(7)	2671(3)	18803(2)	5408(8)
Z	4	2	8	4
T [°C]	298	298	298	298
Radiation	Mo-K_α	Mo-K_α	Mo-K_α	Mo-K_α
ρ_{calcd} [g cm^{-3}]	1.304	1.370	1.247	1.412
μ [mm^{-1}]	0.416	0.673	0.532	0.869
R_1	0.0573[a]	0.0712[b]	0.0795[c]	0.0738[d]
wR_2	0.1561[a]	0.2035[b]	0.1943[c]	0.1889[d]

$w = 1/[\sigma^2(F_o^2) + (aP)^2 + bP]$ and $P = (\max(F_o^2,0) + 2F_c^2)/3$

$R_1 = \Sigma(|F_o| - |F_c|)/\Sigma(|F_o|)$ and $wR_2 = \{\Sigma[w(F_o^2 - F_c^2)^2]/\Sigma[w(F_o^2)^2]\}^{1/2}$

[a] $a = 0.0926$, $b = 18.5641$, for 8260 reflections with $I > 2\sigma(I)$. [b] $a = 0.1349$, $b = 4.3563$, for 5120 reflections with $I > 2\sigma(I)$. [c] $a = 0.1075$, $b = 111.5255$, for 5989 reflections with $I > 2\sigma(I)$. [d] $a = 0.1108$, $b = 34.2934$, for 3829 reflections with $I > 2\sigma(I)$.

were not included in the refinement. Further experimental crystallographic details for **4**: $2\theta_{max} = 45°$, scan speed 1° min^{-1}; scan range 1.6 + $\alpha_{1\alpha2}$ separation; reflections collected/unique/used, 5577/5407 [R_{int} = 0.0442]/5407; 628 parameters refined; $(\Delta/\sigma)_{max} = 0.001$; $(\Delta\rho)_{max}/(\Delta\rho)_{min}$ = 0.896/–0.556 e Å^{-3}; R/R_w (for all data), 0.1198/0.2537. All non-hydrogen atoms were refined anisotropically, except those of the solvate MeCN, which were refined isotropically. Hydrogen atoms on the phenyl rings were introduced at calculated positions as riding on bonded atoms; the rest were not included in the refinement.

CCDC-603113 (for **1**), -603114 (for **2**), -603115 (for **3**), and -603116 (for **4**) contain the supplementary crystallographic data for this paper. These data can be obtained free of charge from The Cambridge Crystallographic Data Centre via www.ccdc.cam.ac.uk/data_request/cif.

Supporting Information (see footnote on the first page of this article): Tables S1, S2, S3, and S4 contain selected bond lengths and angles for compounds **1** **2**, **3**, and **4** respectively. In Figures S1, S2, S7, and S8, error contour plots of J versus J', in Figures S3, S4, S9, and S10, M versus H isotherms at the appropriate temperature, and in Figures S5, S6, S11, and S12, the energy-level plots for the studied compounds are shown. Every figure of each one of the three groups of four figures given above corresponds to each one of the four studied compounds **1**, **2**, **3**, and **4** correspondingly. In Figure S13 the X-band EPR spectrum of a powdered sample of **4** is shown.

Acknowledgments

The Greek General Secretariat of Research and Technology is acknowledged for supporting the present work within the frame of the Competitiveness EPAN 2000–2006, Centers of Excellence no. 25. A. K. B. thanks the Greek State Scholarship Foundation (IKY) for support through a postdoctoral grant. We also thank Dr. D. Stamopoulos for the magnetic measurements.

---

[1] K. Kambe, *J. Phys. Soc. Jpn.* **1950**, *5*, 48–51.

[2] V. A. Gaponenko, M. V. Eremin, Yu. V. Yablokov, *Sov. Phys. Solid State* **1973**, *15*, 909–913.

[3] R. D. Cannon, R. P. White, *Prog. Inorg. Chem.* **1988**, *36*, 195–298.

[4] M. Honda, *J. Phys. Soc. Jpn.* **1993**, *62*, 704–716.

[5] J. Y. Yoon, L. M. Mirica, T. Daniel, P. Stack, E. I. Solomon, *J. Am. Chem. Soc.* **2004**, *126*, 12586–12595.

[6] E. K. Brechin, Y. Yoo, M. Nakomo, J. C. Huffman, D. N. Hendrickson, G. Christou, *Chem. Commun.* **1999**, 783–784.

[7] D. Gatteschi, R. Sessoli, *Angew. Chem. Int. Ed.* **2003**, *42*, 268–297.

[8] S. Gorun, G. C. Papaefthymiou, R. B. Frankel, S. J. Lippard, *J. Am. Chem. Soc.* **1987**, *109*, 4244–4255.

[9] I. Mulyani, A. Levina, P. A. Lay, *Angew. Chem. Int. Ed.* **2004**, *43*, 4504–4507 and references cited therein.

[10] J. Wucher, J. D. Wasscher, *Physica* **1954**, *20*, 721–726.

[11] U. A. Jayasooriya, R. D. Cannon, R. P. White, G. J. Kearley, *Angew. Chem. Int. Ed. Engl.* **1989**, *28*, 930–931.

[12] F. E. Sowrey, C. Tilford, S. Wocadlo, C. E. Anson, A. K. Powell, S. M. Bennington, W. Montfrooij, U. Jayasooriya, R. D. Cannon, *J. Chem. Soc., Dalton Trans.* **2001**, 862–866 and references cited therein.

[13] M. Takano, *J. Phys. Soc. Jpn.* **1972**, *33*, 1312–1317.

[14] T. Murao, *Phys. Lett. A* **1974**, *49*, 33–35.

[15] D. H. Jones, J. R. Sams, R. C. Thomson, *J. Chem. Phys.* **1984**, *81*, 440–447.

[16] N. Uryu, S. A. Friedberg, *Phys. Rev.* **1965**, *140*, 1803–1811.

[17] B. S. Tsukerblat, M. I. Belinski, V. E. Fainzilberg, "Magnetochemistry and spectroscopy of transition metal exchange clusters", in *Soviet Scientific Reviews, Section B* (Chemistry) (Ed.: M. E. Vol'pin), Harwood, Amsterdam, **1987**, pp. 337–481.

[18] Y. V. Rakitin, Y. V. Yablokov, V. V. Zeletontsov, *J. Magn. Reson.* **1981**, *43*, 288–301.

[19] M. Honda, M. Morita, M. Date, *J. Phys. Soc. Jpn.* **1992**, *61*, 3773–3785.

[20] A. Bencini, D. Gatteschi, *EPR of Exchange Coupled Systems*, Springer Verlag, Heidelberg, Germany, **1990**.

[21] C. A. Bates, R. F. Jasper, *J. Phys. C: Solid State Phys.* **1971**, *4*, 2330–2340.

[22] B. S. Tsukerblat, M. I. Belinskii, A. V. Ablov, *Sov. Phys. Solid State (Engl. Transl.)* **1973**, *15*, 19–24.

[23] M. I. Belinskii, B. S. Tsukerblat, A. V. Ablov, *Molecules Molec. Phys.* **1974**, *28*, 283–291.

[24] X. M. Liu, M. P. de Miranda, E. J. L. McInnes, C. A. Kilner, M. A. Halcrow, *Dalton Trans.* **2004**, 59–64.

[25] Y. Sanakis, A. L. Macedo, I. Moura, J. I. G. Moura, V. Papaefthymiou, E. Münck, *J. Am. Chem. Soc.* **2000**, *122*, 11855–11863.

[26] A. Vlachos, V. Psycharis, C. P. Raptopoulou, N. Lalioti, Y. Sanakis, M. Fardis, M. Karayianni, G. Papavassiliou, A. Terzis, *Inorg. Chim. Acta* **2004**, *357*, 3162–3172.

[27] A. K. Boudalis, Y. Sanakis, F. Dahan, M. Hendrich, J.-P. Tuchagues, *Inorg. Chem.* **2006**, *45*, 443–453.

[28] C. Krebs, T. F. Henshaw, J. Cheek, B. H. Huynh, J. B. Broderick, *J. Am. Chem. Soc.* **2000**, *122*, 12497–12506.

[29] C. P. Raptopoulou, V. Tangoulis, V. Psycharis, *Inorg. Chem.* **2000**, *39*, 4452–4459.

[30] C. P. Raptopoulou, Y. Sanakis, A. K. Boudalis, V. Psycharis, *Polyhedron* **2005**, *24*, 711–721.

[31] A. K. Boudalis, Y. Sanakis, C. P. Raptopoulou, A. Terzis, J. P. Tuchagues, S. P. Perlepes, *Polyhedron* **2005**, *24*, 1540–1548.

[32] A. B. Blake, A. Yavari, W. E. Hatfield, C. N. Sethulekshmi, *J. Chem. Soc., Dalton Trans.* **1985**, 2509–2520.

[33] H. Weihe, H. U. Gudel, *J. Am. Chem. Soc.* **1997**, *119*, 6539–6543.

[34] C. Canada-Vilalta, T. A. O'Brien, E. K. Brechin, M. Pink, E. R. Davidson, G. Christou, *Inorg. Chem.* **2004**, *43*, 5505–5521.

[35] C. Wang, K. Fink, V. Staemmler, *Chem. Phys.* **1995**, *201*, 87–94.

[36] S. B. Mukkamala, R. Clerac, C. E. Anson, A. K. Powell, *Polyhedron* **2006**, *25*, 530–538.

[37] G. J. Long, W. T. Robinson, W. P. Tappmeyer, D. L. Bridges, *J. Chem. Soc., Dalton Trans.* **1973**, 573.

[38] M. Luban, F. Borsa, S. Bud'ko, P. Canfield, S. Jun, J. K. Jung, P. Kogerler, D. Mentrup, A. Muller, R. Modler, D. Procissi, B. J. Suh, M. Torikachvili, *Phys. Rev. B* **2002**, *66*, 4407.

[39] M. Fardis, G. Diamantopoulos, M. Karayianni, G. Papavassiliou, V. Tangoulis, A. Konsta, *Phys. Rev. B* **2001**, *65*, 14412 and references cited therein.

[40] D. Procissi, B. J. Suh, A. Lascialfari, F. Borsa, A. Caneschi, A. Cornia, *J. Appl. Phys.* **2002**, *91*, 7173–7175.

[41] G. E. G. Hardeman, N. J. Poulis, W. v. D. Lugt, *Physica (Utrecht)* **1956**, *22*, 48–56.

[42] T. Kohmoto, T. Goto, S. Maegawa, N. Fujiwara, Y. Fukuda, M. Kunitomo, M. Mekata, *Phys. Rev. B* **1994**, *49*, 6028–6039.

[43] T. Goto, T. Koshiba, T. Kubo, K. Agawa, *Phys. Rev. B* **2003**, *67*, 104408.

[44] A. Abragam, B. Bleaney, *Electron Paramagnetic Resonance of Transition Ions*, Clarendon, Oxford, **1970**.

[45] D. Rumbold, G. V. H. Wilson, *J. Phys. Chem. Solids* **1973**, *34*, 1887–1891.

[46] For the analysis of the magnetic susceptibility measurements, monomeric impurities of less than 1% were included for both complexes. At these concentrations these species would give rise to weak signals, which would decrease upon increase of temperature. Such a behavior was observed for a weak signal, denoted by an asterisk in Figure 11, most clearly seen in the spectrum recorded at 4.2 K.

[47] J. R. Pilbrow, *Transition Ion Electron Paramagnetic Resonance*, Clarendon Press, Oxford, **1990**.

[48] F. E. Mabbs, D. J. Machin, *Magnetism and Transition Metal Complexes*, Chapman and Hall, London, **1973**.

[49] *MINUIT Program*, a System for Function Minimization and Analysis of the Parameters Errors and Correlations: F. James, M. Roos, *Comput. Phys. Commun.* **1975**, *10*, 343–367.

[50] a) J. J. Borrás-Almenar, J. M. Clemente-Juan, E. Coronado, B. S. Tsukerblat, *Inorg. Chem.* **1999**, *38*, 6081–6088; b) J. J. Borrás-Almenar, J. M. Clemente-Juan, E. Coronado, B. S. Tsukerblat, *J. Comput. Chem.* **2001**, *22*, 985–991.

[51] E. Fukushima, S. B. W. Roeder, *Experimental Pulse NMR*, Addison-Wesley, Reading, MA, **1981**.

[52] G. M. Sheldrick, *SHELXS-86: Structure Solving Program*, University of Göttingen, Germany, **1986**.

[53] G. M. Sheldrick, *SHELXL-97: Crystal Structure Refinement*, University of Göttingen, Germany, **1997**.

Received: April 5, 2006